Math. Program., Ser. A (2013) 141:383–403
DOI 10.1007/s10107-012-0531-1

FULL LENGTH PAPER

Risk averse elastic shape optimization with parametrized fine scale geometry

Benedict Geihe · Martin Lenz · Martin Rumpf · Rüdiger Schultz

Received: 7 October 2010 / Accepted: 27 February 2012 / Published online: 3 April 2012

Abstract Shape optimization of the fine scale geometry of elastic objects is investigated under stochastic loading. Thus, the object geometry is described via parametrized geometric details placed on a regular lattice. Here, in a two dimensional set up we focus on ellipsoidal holes as the fine scale geometric details described by the semi-axes and their orientation. Optimization of a deterministic cost functional as well as stochastic loading with risk neutral and risk averse stochastic cost functionals are discussed. Under the assumption of linear elasticity and quadratic objective functions the computational cost scales linearly in the number of basis loads spanning the possibly large set of all realizations of the stochastic loading. The resulting shape optimization algorithm consists of a finite dimensional, constraint optimization scheme where the cost functional and its gradient are evaluated applying a boundary element method on the fine scale geometry. Various numerical results show the spatial variation of the geometric domain structures and the appearance of strongly anisotropic patterns.

B. Geihe · M. Lenz · M. Rumpf
Institute for Numerical Simulation, Rheinische Friedrich-Wilhelms-Universität Bonn,
Endenicher Allee 60, 53115 Bonn, Germany
e-mail: benedict.geihe@ins.uni-bonn.de

M. Lenz
e-mail: martin.lenz@ins.uni-bonn.de

M. Rumpf
e-mail: martin.rumpf@ins.uni-bonn.de

R. Schultz (✉)
Fakultät für Mathematik, Universität Duisburg-Essen, Lotharstr. 65,
47057 Duisburg, Germany
e-mail: schultz@math.uni-duisburg.de

Mathematics Subject Classification 90C15 Stochastic Programming · 65N38 Boundary element methods · 65K10 Optimization and variational techniques

1 Introduction

Shape optimization under deterministic loading is a well-developed field in PDE-constrained infinite-dimensional optimization, see e.g. the books [9,33]. In this paper we investigate shape optimization problems for elastic bodies $\mathcal{O} \subset \mathbb{R}^2$ with a special kind of geometry, namely two dimensional perforated plate like domains with possibly many fine holes on a regular lattice (cf. Fig. 1). Motivation for these objects may be drawn from the inner structure of bones, the so-called *substantia spongiosa*. Studies suggest that it forms characteristic structures depending on the typical loads the specific bone usually has to withstand. Also from an engineering view point such materials are interesting because of their mechanical producibility. An alternative model for such a simplified geometry could be to build a lattice of tiny elastic rods, cf. the very early work of Michell [25] dating back to 1904.

The elastic body will be subject to volume and surface loadings which may be fixed but may also vary stochastically over time. The latter is a prevailing issue in many real-world shape optimization problems, in which unlikely but dramatic failures must be appropriately taken into account. The aim of this paper is to derive a finite dimensional constraint optimization scheme to identify the spatially varying, optimal geometric structures under deterministic or stochastic loading conditions. Before we start our analysis, let us briefly review some background and related work.

1.1 The impact of stochastic loading

If we assume stochastic loading the objective function, or shape functional, becomes random. Furthermore, the selection of the shape must be made prior to observing the realizations of the stochastic loading. This requirement, also called nonanticipativity, induces a natural two-stage setting in the optimization problem: In the first stage the decision on the shape is taken. Then stochasticity is unveiled by the realizations of the random loadings. These random realizations, together with the shape, determine

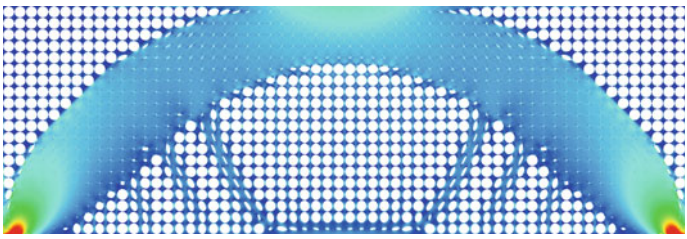

Fig. 1 The optimized fine scale geometry for a bridge type scenario with color-coded von Mises stress distribution (color figure online)

an elasticity PDE whose solution, the displacement, is viewed as the second-stage "decision". Replacing the elasticity PDE by its equivalent variational formulation of minimizing the elastic energy, makes the second-stage "decision" the solution to a second-stage optimization problem.

Together with the nonanticipative shape, the random displacement enters the shape objective which, e.g., could be compliance or deviation from a target shape. From this point of view, the shape functional is a random variable "indexed" by the shapes. The search for an optimal shape thus amounts to finding a "best" random variable. In finite-dimensional two-stage stochastic programming the same setting occurs with Euclidean decision variables taking the roles of the present shapes and displacements, [28–30]. This motivates the following transfer of solution concepts.

First of all, selection of "best" random variables requires some ranking as a prerequisite, for instance assigning real numbers resulting from statistical parameters. If risk neutral, one would take the expected value. If risk averse, some risk measure would be applied.

In the present paper the emphasis is on risk averse optimization models. In various practical applications, there are possible realizations of the random variables that are rather unlikely but which, in case they do occur, have catastrophic consequences. Because of their low probability such scenarios would not have a significant impact on the expectation value. We refine the risk measurement and consider the expectation with respect to suitable nonlinear functions of the cost for each stochastic realization. In particular, we address the *expected excess*, which reflects the expectation of the costs exceeding a given threshold, or the *excess probability*, which measures the probability of a failure, i.e., of a realization with a cost value above the threshold.

1.2 Algorithmic treatment of stochastic shape optimization

Robust optimization offers models and algorithms for optimization under uncertainty if there is no distributional information about uncertain parameters but rather information about their ranges, [8]. This may lead to overly conservative models when enforcing constraints for the full ranges of parameters. As a remedy, robust optimization models with controllable level of conservativeness have been proposed. For robust optimization approaches to shape optimization consult, e.g., [11,12,17,22].

Another means to generalize the single-load assumption in shape optimization is multiload approaches: A fixed (usually small) number of different loading configurations is considered and optimization refers to this set of configurations, see e.g. [3,20,37] and references therein. Then each evaluation of the objective functional requires a separate computation for each of the possible stochastic forces, which renders them infeasible if the set of possible forces is large. In [15,16] shape optimization of elastic bodies under random loading is viewed from the same stochastic programming perspective as in the present paper. In both articles, with [15] confining to risk neutral models, the numerical backbone is level set methods with composite finite elements, in [16] enhanced by topological shape derivatives. Shapes are described as volumetric macroscopic objects with a piecewise smooth boundary. In the present

paper, we consider a fixed domain perforated with a large number of holes, and we optimize the geometry of the holes inside the domain.

1.3 Microscopic structure of optimal materials

Shape optimization problems like the afore mentioned are usually equipped with some volume constraint to avoid trivial solutions. However, if the shape is allowed to evolve freely, these problems are generically ill-posed since microstructures tend to form. As a remedy several regularization techniques have been applied. The simplest way is to use the spatial discretization which, however, leads to highly mesh-dependent results. As a more adequate possibility, one might restrict the number of holes. For a two-dimensional setting existence of a solution to the compliance minimization problem is shown in [10]. Another approach is the penalization of the shape perimeter which (if outside the object there is some weak material instead of void) also results in existence of optimal shapes, see e.g. [6] for a scalar problem and [27] for shape optimization. Finally one might relax the problem and define a set of admissible shapes allowing for microstructures. The so-called homogenization method is a prominent representative of this approach, see [1,2,4]. Here, an indicator function $\chi_{\mathcal{O}}$ is relaxed, such that it can attain any intermediate value between 0 and 1, thus becoming a function describing the relative material density of an elastic body. Restricting the allowed microstructures to sequential laminates, material properties for compliance minimization can be computed explicitly based on homogenization. The fine scale geometries investigated in this paper may be considered a first step towards a two-scale model, where the microstructure is restricted to parametrized geometries as those discussed here.

The paper is organized as follows. In Sect. 2 we briefly describe the geometric properties of the investigated materials and introduce the elastic state equation. We will review shape optimization for the deterministic case in Sect. 3 and define suitable cost functionals for a fixed realization of the loading. The shape derivative will be obtained by using the adjoint technique. Our numerical algorithm is described in Sect. 4 and some illustrative outcomes for the deterministic case will be presented in Sect. 5. Section 6 will then introduce a general class of risk averse shape optimization models, and the examples of expected excess and excess probability as well as proper smooth approximations. We will elaborate on how to use basis loads and a corresponding basis of primal and dual solutions to compute the shape gradient efficiently even in the presence of a large number of realizations of the stochastic loading. Finally we will present our computational results. A short comparison to the setting and the obtained results of Allaire's homogenization method will be drawn in Sect. 7.

2 Shape description and elasticity

Let us first describe the particular fine scale geometry of the elastic bodies $\mathcal{O} \subset \mathbb{R}^2$ investigated in this paper. We consider a fixed domain D perforated with a possibly large number of ellipsoidal holes. Surely, one might consider—with minor modifications of the numerical scheme—other types of parametrized geometric details. We restrict ourselves here to the class of ellipses as a simple class allowing for anisotropic

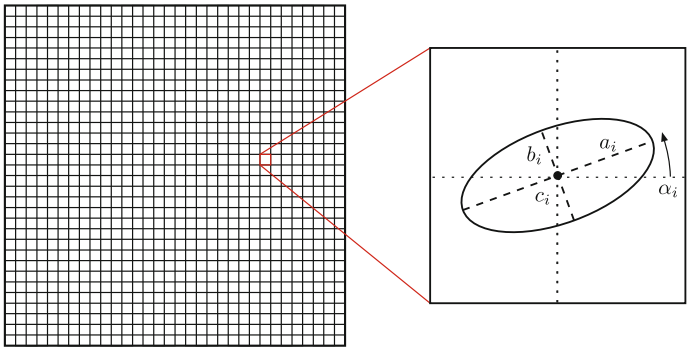

Fig. 2 Sketch of the elastic body and the contained ellipsoidal holes

pattern formation. In contrast to usual shape optimization procedures we do not optimize the outer boundary of D but the fine scale geometric structures inside. We further assume these ellipsoidal holes to be centered at nodes of a regular lattice covering the domain D. Thus we consider N ellipsoidal holes $\mathcal{B}(c_i, \alpha_i, a_i, b_i)$ $(1 \leq i \leq N)$ located in boxes of diameter h and parametrized by a rotation α_i and two scaling factors a_i and b_i for the two semiaxes. The boundary of the ith hole is then given by

$$x(s) = c_i + h \begin{pmatrix} a_i \cos(\alpha_i)\cos(s) - b_i \sin(\alpha_i)\sin(s) \\ a_i \sin(\alpha_i)\cos(s) + b_i \cos(\alpha_i)\sin(s) \end{pmatrix}$$

where the center points c_i fulfill $\frac{c_i}{h} + \frac{1}{2} \in \mathbb{Z}$, cf. Fig. 2. To avoid overlapping of adjacent ellipses or completely vanishing holes, we require the scaling parameters to be bounded, i.e.

$$\delta \leq a_i,\ b_i \leq \frac{1}{2} - \delta \tag{1}$$

with $\delta > 0$ being a small additional offset to prevent numerical instability. The rotation angle however we leave unbounded. Furthermore we suppose the total 2D volume of the elastic body $\mathcal{O} := D \backslash (\bigcup_{i=1,\dots,N} \mathcal{B}(c_i, \alpha_i, a_i, b_i))$ to be fixed. Thus, we impose the equality constraint

$$|D| - \sum_{i=1}^{N} \pi h^2 a_i b_i = V. \tag{2}$$

Any shape $\mathcal{O}$ fulfilling these requirements is called *admissible* and we shortly write $\mathcal{O} \in \mathcal{U}_{\text{ad}}$. Using this description of shapes the resulting shape optimization problem turns into a finite dimensional optimization problem in $\mathbb{R}^{3N}$ with inequality constraints for a_i and b_i and one equality constraint due to the prescribed total 2D volume.

Let us now describe the underlying mechanics of the elastic body. In shape optimization one seeks the realization $\mathcal{O}$ of an elastic body which optimizes a particular mechanical cost functional. Here, we consider the case of linearized elasticity. Given an admissible shape $\mathcal{O} \subset \mathbb{R}^2$ we assume the outer boundary ∂D to be partitioned

into Γ_D on which homogeneous Dirichlet boundary conditions are prescribed and Γ_N on which a sufficiently regular surface load g is applied. The inner boundary of the holes $\partial\mathcal{O}\backslash\partial D$ is considered as a homogeneous Neumann boundary. For the sake of simplicity we neglect volume forces. In case of stochastic loading we consider a random variable ω following a discrete distribution with scenarios ω_i and probabilities π_i with $i = 1, \ldots, N_s$ ($\sum_{i=1}^{N_s} \pi_i = 1$). The applied surface loads will depend on the random variable and we will denote them by $g(\omega)$. For a single realization or a fixed deterministic load the displacement $u : \mathcal{O} \to \mathbb{R}^2$ is determined as the solution of the system of linear partial differential equations

$$-\operatorname{div}(\mathbf{C}\varepsilon(u)) = 0 \tag{3}$$

in $\mathcal{O}$ with $u = 0$ on Γ_D, $(\mathbf{C}\varepsilon(u))n = g$ on Γ_N, and $(\mathbf{C}\varepsilon(u))n = 0$ on $\partial\mathcal{O}\backslash\partial D$. Here, n denotes the outer normal, $\varepsilon(u) = \frac{1}{2}(\nabla u + \nabla u^\top)$ is the linearized strain tensor, and $\mathbf{C} = (\mathbf{C}_{ijkl})_{ijkl}$ the elasticity tensor. Standard results show that for any connected open set $\mathcal{O}$ with Lipschitz boundary and any fixed realization ω the elasticity problem (3) has a unique weak solution $u = u(\mathcal{O}, \omega) \in H^1(\mathcal{O}; \mathbb{R}^2)$ [13,24]. It can be equivalently characterized as the unique minimizer of the quadratic functional

$$E(\mathcal{O}, u, \omega) := \frac{1}{2} A(\mathcal{O}, u, u) - l(\mathcal{O}, u, \omega) \tag{4}$$

on the Hilbert space $H^1_{\Gamma_D}(\mathcal{O}; \mathbb{R}^2) := \{u \in H^1(\mathcal{O}; \mathbb{R}^2) : u = 0 \text{ on } \Gamma_D \text{ in the sense of traces}\}$ with $A(\mathcal{O}, \psi, \theta) := \int_{\mathcal{O}} \mathbf{C}_{ijkl}\varepsilon_{ij}(\psi)\varepsilon_{kl}(\theta)\,\mathrm{d}x$ and $l(\mathcal{O}, \theta, \omega) := \int_{\partial\mathcal{O}} g_i(\omega)\,\theta_i\,\mathrm{d}\mathcal{H}^1$, see [13,19,24] for details. Here and below we implicitly sum over repeated Cartesian indices.

3 Deterministic cost functional and shape derivative

Let us first focus on deterministic shape optimization and derive the corresponding objective functional and shape derivative in a single load case, which will later also serve as ingredients in the stochastic approach.

3.1 Cost functionals

We consider a general objective functional $\mathbf{J}$ which depends on both the shape $\mathcal{O}$ and the resulting elastic displacement $u(\mathcal{O})$, and is given by

$$\mathbf{J}(\mathcal{O}) := J(\mathcal{O}, u(\mathcal{O})) = \int_{\Gamma_N} k(u(\mathcal{O}))\,\mathrm{d}\mathcal{H}^1. \tag{5}$$

Let us emphasize that the surface load is integrated only over the fixed Neumann boundary Γ_N which does not undergo any optimization here. We consider a linear or quadratic function $k(\cdot)$, which will later ensure that even large numbers of stochastic scenarios can be treated efficiently. As particular instances of the general formulation (5), we study the compliance

$$\mathbf{J}_1(\mathcal{O}) := l(\mathcal{O}, u(\mathcal{O})) = \int_{\Gamma_N} g \cdot u(\mathcal{O}) \, \mathrm{d}\mathcal{H}^1 , \tag{6}$$

and the squared difference to a target displacement u_0

$$\mathbf{J}_2(\mathcal{O}) := \frac{1}{2} \int_{\Gamma} |u - u_0|^2 \, \mathrm{d}\mathcal{H}^1 \tag{7}$$

integrated on a subset Γ of the domain boundary ∂D. In the context of the parametrized geometries described in Sect. 2 the objective functional for the deterministic case of a single realization of the loading actually reads

$$\mathcal{J}((\alpha_i, a_i, b_i)_{i=1,\dots,N}) := \mathbf{J}\left(D \backslash \Big(\bigcup_{i=1,\dots,N} \mathcal{B}(c_i, \alpha_i, a_i, b_i) \Big) \right) . \tag{8}$$

3.2 Shape derivative

For the algorithm to be described in Sect. 4, a gradient of the shape functional in the objective has to be computed. This *shape derivative* in direction v, [18], initially takes the form

$$\mathbf{J}'(\mathcal{O})(v) = J_{,\mathcal{O}}(\mathcal{O}, u(\mathcal{O}))(v) + J_{,u}(\mathcal{O}, u(\mathcal{O}))(u'(\mathcal{O})(v)).$$

The vector field v describes variations of the domain $\mathcal{O}$ and will later be induced by variations of the parameters presented in Sect. 2. To avoid an evaluation of $u'(\mathcal{O})(v)$ for any test vector field v the dual or adjoint problem is taken into account. Thereby, the dual solution $p = p(\mathcal{O}) \in H^1_{\Gamma_D}\left(\mathcal{O}; \mathbb{R}^2\right)$ is given as the minimizer of the dual functional

$$E_{dual}(\mathcal{O}, p) := \frac{1}{2} A(\mathcal{O}, p, p) + l_{dual}(\mathcal{O}, p) , \tag{9}$$

with $l_{dual}(\mathcal{O}, p) = \int_{\Gamma_N} k'(u) p \, \mathrm{d}\mathcal{H}^1$. Note that for the compliance objective (6) one obtains $p = -u$. Given p for fixed u and $\mathcal{O}$ the shape derivative of the deterministic cost functional can be rephrased in the following computationally feasible form:

$$\begin{aligned} \mathbf{J}'(\mathcal{O})(v) &= J_{,\mathcal{O}}(\mathcal{O}, u(\mathcal{O}))(v) - l_{dual,\mathcal{O}}(\mathcal{O}, p(\mathcal{O}))(v) + A_{,\mathcal{O}}(\mathcal{O}, u(\mathcal{O}), p(\mathcal{O}))(v) \\ &= \int_{\partial\mathcal{O}} (v \cdot n) \mathbf{C}_{ijkl} \varepsilon_{ij}(u(\mathcal{O})) \varepsilon_{kl}(p(\mathcal{O})) \, \mathrm{d}\mathcal{H}^1 \end{aligned} \tag{10}$$

Finally, we obtain the shape gradient

$$\mathcal{J}'((\alpha_i, a_i, b_i)_{i=1,\dots,N}) = \Big((\partial_{\alpha_j}\mathcal{J}, \partial_{a_j}\mathcal{J}, \partial_{b_j}\mathcal{J})((\alpha_i, a_i, b_i)_{i=1,\dots,N}) \Big)_{j=1,\dots,N}$$

as a vector in $\mathbb{R}^{3N}$.

4 The numerical algorithm in the deterministic case

This section is devoted to the numerical optimization algorithm. We will briefly review the boundary element method (BEM) which is taken into account to compute the primal and dual solutions as minimizers of (4) and (9) and comment on some technical issues regarding the implementation.

4.1 The boundary element method

Main ingredient of the boundary element method is the fundamental solution of the investigated elasticity model [14]. It uses the complex logarithm and thus requires to map points $x \in \mathbb{R}^2$ onto the complex plane via the linear function $z(x) = x_1 + p\, x_2$ for a complex constant p. With A_{kn}, N_{nj}, D_{ijn}, d_{ti} being further appropriately chosen constants, the fundamental solution and its normal derivative are given by

$$u^*_{ki} = \frac{1}{2\pi} \sum_t \Re \left\{ \sum_n A_{kn} N_{nt} \ \ln\left(z_n(x-y)\right) \right\} d_{ti},$$
$$v^*_{ki} = -\frac{1}{2\pi} \sum_{j,t} \Re \left\{ \sum_n \frac{D_{kjn} N_{nt}}{z_n(x-y)} \right\} d_{ti}\, n_j.$$

We now consider the equation $A(\mathcal{O}, u, \theta) = l(\mathcal{O}, \theta, \omega)$, apply Green's formula, substitute θ by the fundamental solutions u^*_i and arrive at

$$u_i(x) = \int_{\partial\mathcal{O}} (\mathbf{C}\varepsilon(u)n) \cdot u^*_i \, \mathrm{d}\mathcal{H}^1(y) - \int_{\partial\mathcal{O}} \left(\mathbf{C}\varepsilon(u^*_i)n\right) \cdot u \, \mathrm{d}\mathcal{H}^1(y). \tag{11}$$

For $x \in \partial\mathcal{O}$ these are singular integrals to be defined in an appropriate way. (For details we refer to [21].) Finally, for the displacement u on $\partial\mathcal{O}$ and for the normal tension $\sigma_n = \mathbf{C}\varepsilon(u)n$ on $\partial\mathcal{O}$ one obtains from (11) the integral equation

$$u = U[\sigma_n] - V[u], \tag{12}$$

where U is a so called *single layer operator* and V a *double layer operator*. For the discretization we consider a polygonal approximation $\mathcal{O}_h$ of the domain $\mathcal{O}$ and on the boundary $\partial\mathcal{O}_h$ we fix a set $\mathcal{N}_h$ of *collocation points* ξ_i and approximate u as well as σ_n via linear interpolation of corresponding values. Effectively, the collocation points depend on the free parameters c_i, α_i, a_i, and b_i of the ellipses. We now require (12) to hold for every ξ_i leading to a linear system of equations for the values of the displacements and the normal tensions at each collocation point. The boundary integral operators U and V applied to affine basis functions on $\partial\mathcal{O}$ can be computed analytically so that our algorithm does not require any numerical quadrature. Notice that we typically consider mixed boundary value problems requiring a rearrangement of the discretized analogon of (12) according to known and unknown displacements and tensions.

In the BEM approach displacements and tensions need only be computed on the polygonal boundary. Furthermore, the objective functionals (6) and (7) and the corresponding shape derivatives in (10) are also phrased as boundary integrals. To evaluate these integrals however full gradients ∇u and ∇p are required whereas we only have discrete approximations of the normal stresses at our disposal so far. To reconstruct the full gradient $\nabla u = \mathcal{P}_{T_x\partial\mathcal{O}}\,\nabla u + \partial_n u\; n$ (with $\mathcal{P}_{T_x\partial\mathcal{O}}$ being the orthogonal projection onto the tangent space $T_x\partial\mathcal{O}$ at $x \in \partial\mathcal{O}$) we use piecewise constant approximations of the missing tangential derivative based on a piecewise linear reconstruction of the displacement on edges of $\partial\mathcal{O}_h$ for given collocation data on nodes. Finally, the normal derivative can be recovered by solving a 2×2 system of linear equations for each collocation point resulting from $(\mathbf{C}\varepsilon(u))n = \sigma_n$ and the given tangential derivative $\mathcal{P}_{T_x\partial\mathcal{O}}\,\nabla u$.

4.2 Implementation

As already stated in Sect. 2 we finally have to solve a finite dimensional nonlinear optimization problem in which the $3\,N$ parameters $(\alpha_i, a_i, b_i)_{i=1,\dots,N}$ of the ellipsoidal holes appear as variables and additional constraints are given by (1) and (2). The treatment of such constrained optimization problems is a classical and well-developed field, see e.g. [26]. Here, we rely on the software package `Ipopt` [35,36] which implements a Primal-Dual Interior Point Filter Line Search algorithm. The considered cost functionals are in general non-convex. Thus, we expect to compute only local minimizers and thus at least locally optimal geometric domain patterns using such an SQP-type method.

We employ the `C++` interface of `Ipopt` and supply routines for the evaluation of our (stochastic) cost functionals and the corresponding derivatives. For the Hessian we make use of the built-in approximation by the *SR1* update strategy. This especially guarantees positive definiteness which is of importance here because the Hessian becomes singular if the scaling parameters for one cell are equal and the local geometry is invariant with respect to the rotation parameter. In Fig. 3 we plot the objective functional over the descent iterations of the algorithm. Notice that the objective drops slightly below the final value at some point. This is due to the filter approach which accepts an optimization step if either the cost or the constraint violation is improved.

For the solution of the primal and dual problems as well as for the management of our domain boundary we apply a `C++` library [23] taylored to 2D BEM applications. A typical optimization problem like in Fig. 4 below comes with 1,200 parameters to be optimized and about 5,000 collocation points, leading to about 10,000 degrees of freedom. Around 40 relaxation steps are performed by `Ipopt` until convergence is detected. Each step on average requires 1.2 evaluations of the cost functional and one gradient evaluation. As cached solutions are retrieved not every evaluation of the cost functional requires the solution of the underlying elastic system. However the corresponding matrix is dense and we have to use a direct solver—in the case currently QR-decomposition—amounting to about 98 % of the overall CPU time of 30 hours on moderate desktop hardware. The computational complexity can be drastically

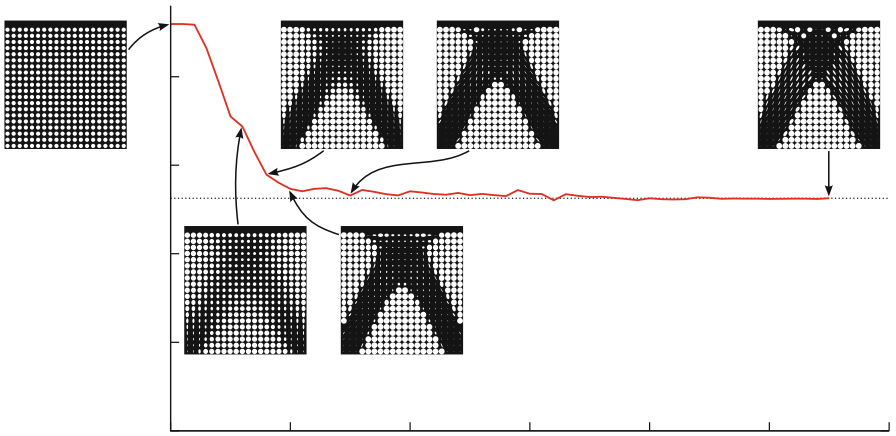

Fig. 3 Objective during optimization by `Ipopt`. The final value is indicated by the *dashed line*

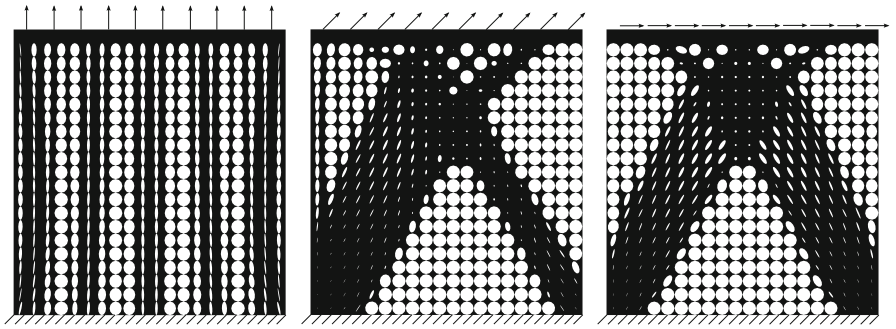

Fig. 4 Different deterministic loadings and the resulting locally optimal shapes

reduced by using hierarchical preconditioning of the discretized integral equation via the concept of H-matrices. We refer to [23] where the integration of the `AHMED` library into our framework is discussed. The `AHMED` library provides an implementation of the adaptive cross approximation for the construction of hierarchical matrices [7]. Based on the measurements in [23] we may expect a speedup of factor 200.

In the result sections we will also show stress plots of our investigated domains (cf. Fig. 5). Solely for this post processing purpose a triangulation of the computational domain is generated using the software `Triangle` [31,32]. At each interior vertex the linearized strain tensor is then computed using (11). Indicator values are finally color-coded and interpolated on each triangle using a self-written software based on `The Visualization Toolkit` (`VTK`).

5 Deterministic structure optimization

As a counterpart to subsequent discussion of stochastic models and the optimal shapes in a risk averse setup let us at first present some illustrative outcomes of the optimization algorithm from Sect. 4 for a carrier plate and a cantilever under deterministic loadings.

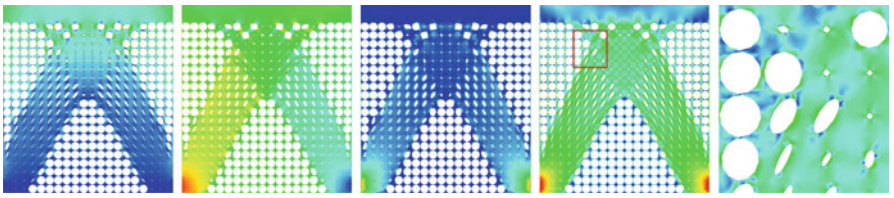

Fig. 5 Different types of loading indicators: determinant of the displacement gradient $\det \nabla u$, trace of the displacement gradient $\operatorname{tr} \nabla u$, integrand of the compliance energy $\mathbf{J}_1$, von Mises stress and an additional blow-up of the *square* marked in *red* (color figure online)

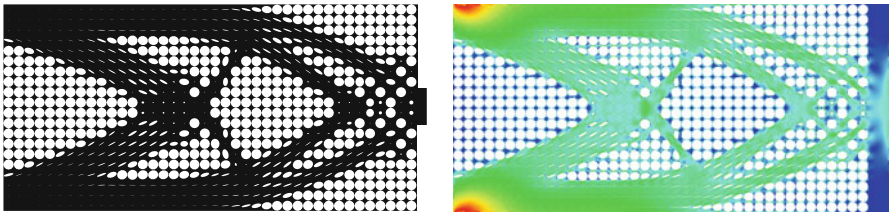

Fig. 6 Locally optimal fine scale structure of a cantilever, color-coded with the von Mises stresses on the *right* (color figure online)

5.1 Carrier plate

Consider a 2D carrier plate $D = [0, 1] \times [0, 1]$ with 20×20 ellipsoidal holes on a regular lattice. The shape to be optimized is a supporting construction between a fixed floor plate, where homogeneous Dirichlet boundary conditions are prescribed, and an upper plate, where the loading attacks. Everywhere else, i.e. especially on ellipses' boundaries, homogeneous Neumann boundary values are assumed. Figure 4 shows three different loading scenarios and the corresponding outcomes of our shape optimization algorithm. In Fig. 5 different types of loading indicators for the shearing case are displayed.

5.2 Cantilever

As a second application, we study shape optimization of a 2D cantilever. Here $D = [0, 2] \times [0, 1]$, now perforated with 40×20 holes and we aim at modeling a cantilever that is fixed on the left side and has a deterministic downward pointing force applied on a centered, small part of the boundary on the right. Figure 6 displays the result together with the von Mises stress.

Let us point out that, although the above shapes have a fixed topology and lack flexibility to evolve when compared to the level-set description in [15,16], one can clearly recognize characteristic structures in the obtained results. Relatively sharp interfaces between "void" and "non-void" regions are formed and small elongated ellipses are approximately aligned with the main loading directions in the trusses.

6 Risk averse stochastic structure optimization

We now turn to shape optimization under stochastic loadings. The aim is to find shapes of elastic bodies withstanding in some "best way" not just an individual load but rather a multitude of loads arising with certain probabilities. When exposed to some fixed shape $\mathcal{O}$, the stochastic loading induces stochastic displacements and finally, in (5), stochastic costs $\mathbf{J}(\mathcal{O}, \omega)$. Thus, for any admissible shape $\mathcal{O}$, the optimization criterion yields a random cost variable $\mathbf{J}(\mathcal{O}, \omega)$. Shape optimization then is rephrased as minimization over the family of random cost variables $\{\mathbf{J}(\mathcal{O}, \omega) \,:\, \mathcal{O} \in \mathcal{U}_{\text{ad}}\}$. Minimizing over this set requires a concept of how to rank its members. In the present paper this is achieved by applying statistical parameters.

6.1 Expected value

The most apparent approach might be to consider the expected value $\mathbf{Q}_{\mathbb{E}}(\mathcal{O}) := \mathbb{E}\left(J\left(\mathcal{O}, \omega\right)\right)$ which was investigated in a classical shape optimization setup in [15]. This model already yields significantly different results compared to optimization of the (deterministic) expected value of the applied loadings. Still it is risk neutral; critical realizations of $\mathbf{J}(\mathcal{O}, \omega)$ with little impact on the expected value are given only little priority.

To remedy this, a risk averse point of view was introduced for macroscopic geometry optimization in [16] which we will pick up here in the context of fine scale structure optimization. Minimization of the expectation of the objective function is replaced by minimization of the expectation of suitable nonlinear transformations of the objective function

$$\min \left\{ \mathbf{Q}(\mathcal{O}) := \mathbb{E}\left(q\left(\mathbf{J}(\mathcal{O}, \omega)\right)\right) = \sum_{i=1}^{N_s} \pi_i q\left(\mathbf{J}(\mathcal{O}, \omega_i)\right) \,:\, \mathcal{O} \in \mathcal{U}_{\text{ad}} \right\}, \tag{13}$$

where $q : \mathbb{R} \to \mathbb{R}$ is a monotonically increasing function. Here, we recall that ω_i are stochastic realizations with probabilities π_i for $i = 1, \ldots, N_s$. For $q(t) = t$ this obviously reduces to minimizing the expected value. In the following we will however consider two different risk measures, namely the *expected excess* and the *excess probability*.

6.2 Expected excess

Let us assume we are given a threshold value $\eta \in \mathbb{R}$ reflecting some critical level of loading. The expected excess then arises by using the weight function $q(t) = \max\{t - \eta, 0\}$:

$$\mathbf{Q}_{\text{EE}_\eta}(\mathcal{O}) := \mathbb{E}\left(\max\{\mathbf{J}(\mathcal{O}, \omega) - \eta, 0\}\right). \tag{14}$$

Effectively this expectation "ignores" realizations ω whose cost is below the threshold, thereby paying more attention to those exceeding it. To improve numerical tractability we replace the max-function by a smooth approximation

$$\mathbf{Q}^{\epsilon}_{\mathrm{EE}_\eta}(\mathcal{O}) := \mathbb{E}\left(q^{\epsilon}(\mathbf{J}(\mathcal{O},\omega))\right)$$

where $q^{\epsilon}(t) := \frac{1}{2}\left(\sqrt{(t-\eta)^2+\epsilon} + (t-\eta)\right), \epsilon > 0.$

6.3 Excess probability

If, for a given threshold η, it only matters whether the cost threshold η is exceeded or not, one ends up with the weight function $q(t) = H(t-\eta)$ with H denoting the Heaviside function defined by $H(t) = 1$ for $t > 0$ and 0 otherwise. The excess probability then reads:

$$\mathbf{Q}_{\mathrm{EP}_\eta}(\mathcal{O}) := \mathbb{E}\left(H\left(\mathbf{J}(\mathcal{O},\omega) - \eta\right)\right). \tag{15}$$

In fact, this objective just adds up the probabilities of the realizations exceeding the threshold. A suitable smooth approximation is given by

$$\mathbf{Q}^{\epsilon}_{\mathrm{EP}_\eta}(\mathcal{O}) := \mathbb{E}\left(H^{\epsilon}(\mathbf{J}(\mathcal{O},\omega))\right)$$

for $H^{\epsilon}(t) := \left(1 + e^{-\frac{2(t-\eta)}{\epsilon}}\right)^{-1}$.

6.4 Evaluation of objectives and derivatives

To be able to evaluate the various objective functionals and their gradients the primal and dual solutions $u(\mathcal{O},\omega) \in H^1_{\Gamma_D}(D;\mathbb{R}^2)$ and $p(\mathcal{O},\omega) \in H^1_{\Gamma_D}(D;\mathbb{R}^2)$ need to be known for all ω. However under our requirement that $k(\cdot)$ is a linear or quadratic function, we can employ a significant shortcut for $N_s \gg 1$, which was broken down in [15]. The crucial point is that the dependence of the primal and dual solution on ω is linear. We can therefore consider a "basis" of (deterministic) surface loads $g_1, \ldots, g_K$ and write the actual loads $g(\omega)$ as linear combinations

$$g(\omega) = \sum_{j=1}^{K} c_j^g(\omega) g_j$$

with uncertain coefficients $c_j^g(\omega) \in \mathbb{R},\ j = 1, \ldots, K$. Doing so we only need to solve as many PDEs as there are basis forces, which will significantly reduce the computing cost in case $N_s \gg K$. Let us assume we obtain primal solutions u^j for surface loads

$g := g_j$ and $j = 1, \ldots, K$. Then for linearity reasons

$$u(\mathcal{O}; \omega) := \sum_{j=1}^{K} c_j^g(\omega) u^j \tag{16}$$

is the unique minimizer of (4) with surface load $g := g(\omega)$. If we additionally assume $\sum_{j=1}^{K} c_j^g(\omega) = 1$—which can always be achieved by altering the basis forces appropriately—a similar relation holds for the adjoint solution. Here it is important that because of k depending linearly or quadratically on u, the dependence of $k_{,u}$ on u is linear. Therefore, given the dual solutions for the basis forces p^j one obtains

$$p(\mathcal{O}; \omega) := \sum_{j=1}^{K} c_j^g(\omega) p^j \tag{17}$$

as the unique minimizer of (9) belonging to $u(\mathcal{O}; \omega)$.

With the primal and dual solutions at hand we can compute the stochastic shape derivative of the objective functionals. Because of the transformations q the chain rule has to be applied and we finally obtain

$$(\mathbf{Q}_{\mathbb{E}})'(\mathcal{O})(v) = \mathbb{E}\left(\mathbf{J}'(\mathcal{O}, \omega)(v)\right) = \sum_{i=1}^{N_s} \pi_i J'(\mathcal{O}; \omega_i)(v),$$

$$\left(\mathbf{Q}^{\epsilon}_{\mathrm{EE}_\eta}\right)'(\mathcal{O})(v) = \sum_{i=1}^{N_s} \frac{\pi_i}{2} \mathbf{J}'(\mathcal{O}; \omega_i)(v) \left(\frac{\mathbf{J}(\mathcal{O}, \omega_i) - \eta}{\sqrt{(\mathbf{J}(\mathcal{O}, \omega_i) - \eta)^2 + \epsilon}} + 1 \right),$$

$$\left(\mathbf{Q}^{\epsilon}_{\mathrm{EP}_\eta}\right)'(\mathcal{O})(v) = \sum_{i=1}^{N_s} \frac{2}{\epsilon} \pi_i \mathbf{J}'(\mathcal{O}, \omega_i)(v)\, e^{-\frac{2}{\epsilon}(\mathbf{J}(\mathcal{O}, \omega_i) - \eta)} \left(1 + e^{-\frac{2}{\epsilon}(\mathbf{J}(\mathcal{O}, \omega_i) - \eta)}\right)^{-2}.$$

To assemble the cost functional and the gradient of the cost in the optimization algorithm one has to compute for the current discretized domain $\mathcal{O}_h$ once the K discretized primal base deformations $U^j(\mathcal{O}_h)$ and the corresponding discretized dual base states $P^j(\mathcal{O}_h)$. From these, we can efficiently compute the effective deformations $U(\mathcal{O}, \omega_i)$ and the effective dual states $P(\mathcal{O}, \omega_i)$ for a possibly very large set of scenarios and then evaluate the stochastic shape derivative.

6.5 Results

In the remainder of this section we will present results for two applications already considered with respect to macroscopic geometry optimization in [16]. The first one features two fixed bearings which are loaded in different directions from the top whereas the bottom of the investigated domain is kept fixed. We consider the compliance cost and search for the optimal construction of trusses underneath these bearings. The second one models a cantilever fixed on the left hand side with a vertical load distribution applied on the lower boundary. Here we look for an optimal design minimizing the

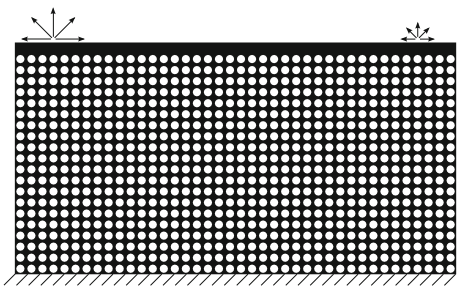

Fig. 7 Initial configuration with a sketch of the applied stochastic loading

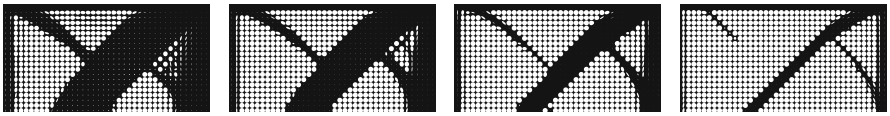

(a) $V = |D| - 0.3^2\pi$ **(b)** $V = |D| - 0.35^2\pi$ **(c)** $V = |D| - 0.4^2\pi$ **(d)** $V = |D| - 0.45^2\pi$

Fig. 8 Results for optimization with respect to the expected value for different values of volume V

displacement of the loaded surface. All computations are performed on the domain $D = [0, 2] \times [0, 1]$ perforated with 40×20 ellipsoidal holes and start from the initial configuration shown in Figs. 7 and 12 respectively. To ensure an effective minimization of the stochastic cost functional, it turned out that in the excess probability case a substantial regularization is indispensable. In fact, here we have chosen the regularization parameter ϵ such that the transition range between $H_\epsilon = 0.2$ and $H_\epsilon = 0.8$ takes place on an approximate fraction of 0.3 of the total cost range in the application. The regularization in the expected excess model is less critical. Indeed, we have chosen values for ϵ between 10^{-5} and 10^{-8}.

6.5.1 Trusses underneath two fixed bearings

The loading scenario we consider here is depicted in Fig. 7. Five loads act on the right bearing with probability 0.19. Corresponding loads on the left bearing are twice as strong but only appear by a chance of 0.01. These loads are supposed to be the critical ones. However, on average, they only have minor impact. All of them can be combined using four basis forces consisting of the two unit vectors on top of the left and the right bearing.

In Fig. 8 we compare the shapes which (locally) minimize the expected value of the compliance cost functional for different volumes V. As expected the results differ significantly from those that would have been obtained when optimizing for the expected value of the applied loadings. In the latter case the resulting shape would actually consist of two vertical trusses which have a very weak response to transversal loadings.

Next, we investigate risk averse shape optimization for this setting. In Fig. 9 a family of optimized shapes for varying excess parameter η is depicted. Here and below we used $V = |D| - 0.375^2\pi$ for the volume constraint. We experimentally observe a continuous evolution of the geometry with η, even though each of the computations has

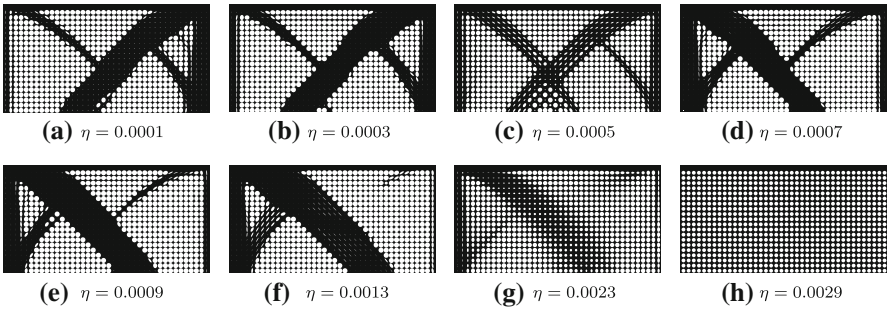

Fig. 9 A sequence of results for the optimization with respect to the expected excess for varying η. The underlying loading is shown in Fig. 7

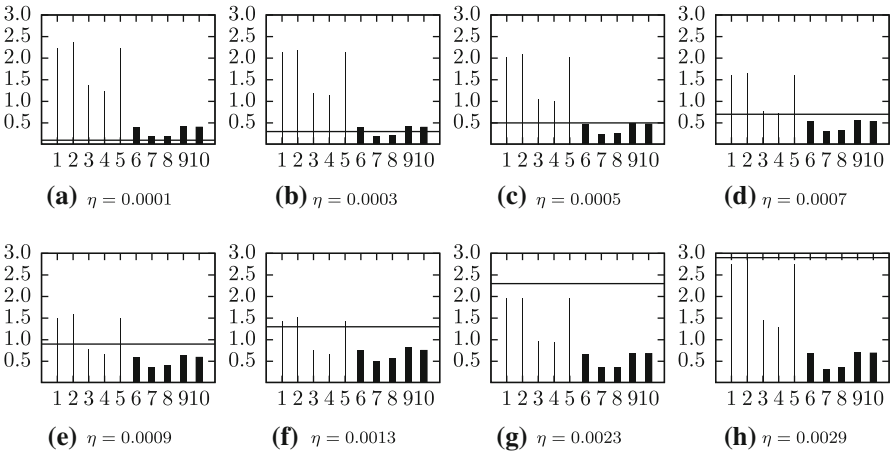

Fig. 10 Objective values (scaled by 10^3) are rendered with *bar* charts for the shapes in Fig. 9. The *bar thickness* is chosen proportional to the probability of the corresponding scenario

been restarted from the same initial configuration (cf. Fig. 7). For small values of η the observed shapes are still close to the one obtained when optimizing for the expected value. However as the threshold parameter is increased scenarios with low objectives, i.e. the ones on the right, become more and more disregarded, see also Fig. 10. Because of the regularized formulation of the stochastic cost functional they are still taken into account but only with decreasing weight. As a consequence less "material" is needed for these realizations permitting more flexibility for the specific optimization of the critical scenarios on the left bearing. Beyond a certain threshold value even those are no longer relevant, which becomes apparent in the last two images.

We now turn to the excess probability risk measure. Albeit somewhat related to the expected excess different phenomena can be observed. Because the amount of excess is completely irrelevant, low weighted scenarios with high objective values (the ones on the left) are considered to be "lost" for small values of η, thereby leaving the left part of the computational domain unoptimized (cf. Fig. 11). Indeed one observes that

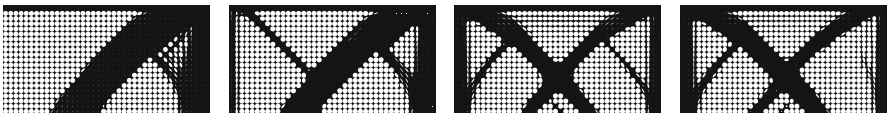

(a) $\eta = 0.0009$ **(b)** $\eta = 0.0011$ **(c)** $\eta = 0.0021$ **(d)** $\eta = 0.0023$

Fig. 11 A sequence of results for the optimization with respect to the excess probability for varying η. The underlying loading is shown in Fig. 7

objective values for the 5 scenarios on the left increase while the algorithm focuses on pushing the costs for the high-probability realizations on the right below the threshold.

To sum up we remark that the expected value causes a weighted averaging over all optimal shapes for single scenarios. In contrast for the expected excess there is no further need to optimize scenarios whose objective values have already been pushed below the threshold thereby allowing more flexibility for cost reduction of the other realizations. Finally the excess probability only addresses how likely scenarios exceed the threshold leading to full ignorance of scenarios high above. As to the used regularization for the risk measures $\mathbf{Q}^{\epsilon}_{\mathrm{EE}_\eta}$, $\mathbf{Q}^{\epsilon}_{\mathrm{EP}_\eta}$ one has to bear in mind that the threshold behavior discussed above is smeared out. Cost reduction of single scenarios in the vicinity of η is therefore always favorable.

6.5.2 Cantilever with vertical loading distribution

Our second investigated example deals with a cantilever construction fixed at a Dirichlet boundary on the left whose lower boundary is subject to vertical loads with a random spatial distribution. We use five basis loads and build up two different random loading schemes, each consisting of ten scenarios with varying probability (cf. Fig. 12). The two different loading schemes have the same expected value of the loads (cf. bottom sketch of the load distribution in both loading schemes of Fig. 12). Their main difference is that the first configuration is characterized by a single, high probability load scenario on the right end of the lower beam whereas the second configuration has a single, high probability load scenario acting on the left.

For this example we use the deflection of the lower beam ((7) with $u_0 = 0$) as objective functional leading to an adjoint problem truly different from the primal problem. We have chosen $V = |D| - 0.375^2\pi$ for the volume constraint.

In this example the basis loads are applied spatially separated and only positive weights are used for building up the load for each scenario. Therefore no cancellation effect as in our first example can occur and the resulting shapes for the expected value measure differ only slightly from the one obtained by optimizing for the expected value of the loads. On the other hand the stochastic loadings are applied on a continuous part of the boundary which seems to bring up a more complicated energy landscape than in the example before. Let us emphasize that we are able to search only for local minima and that we started all our computations from the same initial domain shown in Fig. 12. In contrast to the first example, we are dealing with at least one dominating scenario in each of the two schemes leading to a broader range of objective values. We therefore drop an analysis of the shapes for varying threshold η here and use this

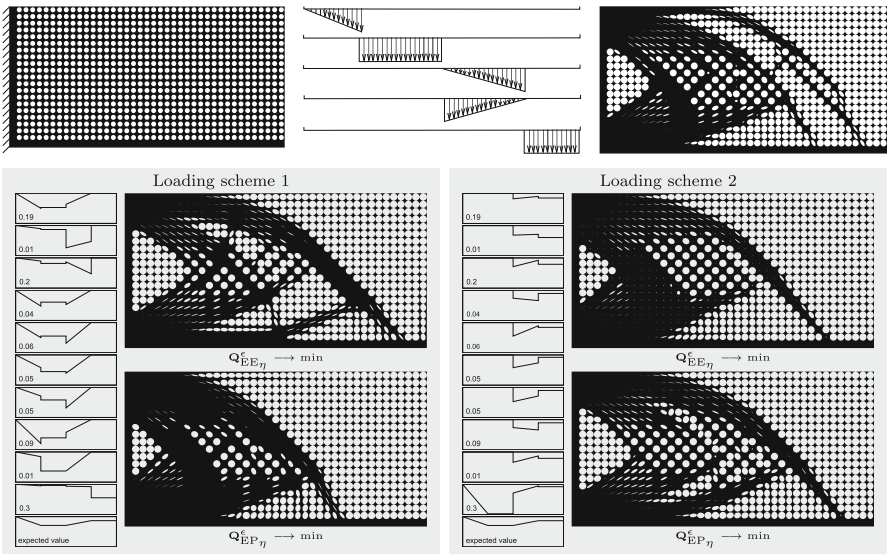

Fig. 12 *Top* Initial configuration, basis loads on lower boundary and result for deterministic optimization with respect to the expected value of the applied loadings. *Bottom* Sketch of the loadings for the two different loading schemes consisting of 10 scenarios each and results of the optimization with respect to the expected excess (*top*) and excess probability (*bottom*) for $\eta = 1$

example to again underline the differences of the considered risk measures for $\eta = 1$ being fixed.

For the first loading scheme all scenarios except the last one have an objective value close to the threshold already for the initial configuration. Optimization with respect to the expected excess therefore focuses on improving the structure for the scenario loading the right end of the lower boundary. This especially results in a thicker truss on the right when compared to the outcome of the optimization with respect to the expected value (cf. Fig. 12). For the excess probability however the last scenario is out of reach and therefore "lost". Because of the regularization parameter several other scenarios still have influence on the overall cost. Among these scenarios 1 and 3 have significantly higher probabilities than the rest and optimization is therefore basically carried out for their loads.

For the second loading scheme scenario 2 imposes a high load on the right end of the lower border and thereby clearly exceeds the threshold. Its probability however is among the lowest and so it enters the expected excess only with a negligible weight. The optimization is rather steered by the dominating scenario 10 leading to massive support in the left area of the domain. This scenario also characterizes the outcome for the excess probability risk measure. Like in the first scheme, scenario 2 gets very low priority in the optimization. High probability scenarios near the threshold are again considered for optimization showing a structure similar to the one obtained for the expected excess. However due to the fact that the amount of excess is not crucial, scenario 10 is less dominant resulting in a less dense structure than before.

To conclude we present a cross-check of the results for each scheme in the following table which lists values for each of the considered risk measures on each of the different domains obtained by running our optimization algorithm for the different cost functionals.

	$\mathbf{Q}_{\mathbb{E}}(\cdot)$	$\mathbf{Q}_{\mathrm{EE}_\eta}(\cdot)$	$\mathbf{Q}_{\mathrm{EP}_\eta}(\cdot)$
Loading scheme 1			
$\mathcal{O}_{\mathbb{E}}$	1.177	0.402	0.466
$\mathcal{O}_{\mathrm{EE}_\eta}$	1.205	0.377	0.511
$\mathcal{O}_{\mathrm{EP}_\eta}$	1.501	0.808	0.418
Loading scheme 2			
$\mathcal{O}_{\mathbb{E}}$	1.102	0.279	0.495
$\mathcal{O}_{\mathrm{EE}_\eta}$	1.127	0.259	0.532
$\mathcal{O}_{\mathrm{EP}_\eta}$	1.181	0.384	0.483

7 A brief comparison of perforated materials and laminates

As mentioned earlier our computed shape optimization results reveal two interesting phenomena: On the one hand one can observe the formation of macroscopic geometries represented by the region with holes with radii below $(\frac{1}{2} - \delta)h$. On the other hand fine anisotropic structures are developing within these (macroscopic) shapes. Although our model presented here aims at allowing many fine holes it is still a one-scale approach. However when looking at the results (e.g. Fig. 4) a periodic pattern with respect to the shape of the ellipsoidal holes attracts attention and a two-scale approach assuming a periodic mircostructure seems natural.

Such a setting is related to the homogenization method introduced by Allaire [1] in the field of shape optimization. The main difference being the type of admissible microstructure. In [2,4] nested sequential laminates as microstructure were taken into account. The resulting macroscopic material properties can be computed explicitly and hence a relaxing variational approach could be used on the macroscale. Indeed, optimization is then carried out for the lamination directions and the relative material density. In particular, for a single fixed load rank-2 sequential laminates with the lamination directions aligned with the stress eigendirections are known to be optimal for compliance minimization in 2D. However, different from the perforated domains they are difficult to manufacture. For this reason, optimization is often followed by a postprocessing step in which composite regions are penalized. The outcomes reveal similar structures to the ones we observed for our results, compare for instance Fig. 1 with [1, Fig. 5.28, p. 399]. Furthermore it seems that the orientations of the ellipses' semi-major axes also aligned with the main directions of stress. Similar observations for numerical optimization results have been made e.g. in [34].

In the context of the homogenization method employing laminates [5] formally derives an interesting relation: If the Lagrange multiplier related to the volume constraint tends to infinity the relaxed optimization problem is asymptotically equivalent to the Michell truss problem [25]. In this setting one optimizes a network made up of arbitrarily many hinge joints connected by elastic rods. It is assumed that the cross-section of the rods is proportional to the tensile or compressive stress the rod can withstand. To achieve an optimal design the rods have to be aligned with the principal

stress directions and have to be able to bear a load proportional to the corresponding principal stresses. Thus, searching for the lightest structure one has to minimize the integral over the sum of the principal stresses. Indeed, up to material constants this minimization problem coincides with the limit of the relaxed formulation in the context of laminates in [5]. It is therefore not surprising that the results obtained here share characteristic features with optimal Michell truss networks.

Acknowledgments This work was supported by the Deutsche Forschungsgemeinschaft through the Schwerpunktprogramm 1253 *Optimization with Partial Differential Equations*.

References

1. Allaire, G.: Shape Optimization by the Homogenization Method, vol. 146. Springer Applied Mathematical Sciences, Berlin (2002)
2. Allaire, G., Bonnetier, E., Francfort, G., Jouve, F.: Shape optimization by the homogenization method. Numerische Mathematik **76**, 27–68 (1997)
3. Allaire, G., Jouve, F.: A level-set method for vibration and multiple loads structural optimization. Comput. Methods Appl. Mech. Eng. **194**(30–33), 3269–3290 (2005)
4. Allaire, G., Jouve, F., Maillot, H.: Topology optimization for minimum stress design with the homogenization method. Struct. Multidisc. Opt. **28**, 87–98 (2004)
5. Allaire, G., Kohn, R.V.: Optimal design for minimum weight and compliance in plane stress using extremal microstructures. Euro. J. Mech. Solids **12**(6), 839–878 (1993)
6. Ambrosio, L., Buttazzo, G.: An optimal design problem with perimeter penalization. Calculus Variations Partial Differ. Equ. **1**, 55–69 (1993)
7. Bebendorf, M.: Hierarchical Matrices: A Means to Efficiently Solve Elliptic Boundary Value Problems, vol. 63 of Lecture Notes in Computational Science and Engineering (LNCSE). Springer, Berlin, 2008. ISBN 978-3-540-77146-3
8. Ben-Tal, A., El-Ghaoui, L., Nemirovski, A.: Robust Optimization. Princeton University Press, Princeton (2009)
9. Bendsøe, M.P.: Optimization of structural topology, shape, and material. Springer, Berlin (1995)
10. Chambolle, A.: A density result in two-dimensional linearized elasticity, and applications. Arch. Ration. Mech. Anal. **167**(3), 211–233 (2003)
11. Cherkaev, A., Cherkaeva, E.: Optimal design for uncertain loading conditions. In: V. Berdichevsky, V. Jikov, G. Papanicolaou (eds.) "Homogenization", vol. 50 of Series on Advances in Mathematics for Applied Sciences, pp. 193–213 World Scientific, Singapore (1999)
12. Cherkaev, A., Cherkaeva, E.: Principal compliance and robust optimal design. J. Elast. **72**, 71–98 (2003)
13. Ciarlet, P.G.: Mathematical Elasticity Volume I: Three-Dimensional Elasticity, vol. 20. Studies in Mathematics and its Applications, North-Holland (1988)
14. Clements, D., Rizzo, F.: A method for the numerical solution of boundary value problems governed by second-order elliptic systems. IMA J. Appl. Math. **22**, 197–202 (1978)
15. Conti, S., Held, H., Pach, M., Rumpf, M., Schultz, R.: Shape optimization under uncertainty—a stochastic programming perspective. SIAM J. Optim. **19**, 1610–1632 (2009)
16. Conti, S., Held, H., Pach, M., Rumpf, M., Schultz, R.: Risk averse shape optimization. SIAM J. Cont. Optim. **49**(3), 927–947 (2011)
17. de Gournay, F., Allaire, G., Jouve, F.: Shape and topology optimization of the robust compliance via the level set method. ESAIM: Cont. Optim. Calculus Var. **14**, 43–70 (2007)
18. Delfour, M.C., Zolésio, J.: Shapes and geometries: analysis, differential calculus and optimization. Adv. Des. Control 4. SIAM, Philadelphia (2001)
19. Evans, L.C.: Partial Differential Equations, vol. 19. AMS Graduate Studies in Mathematics (2002)
20. Guedes, J.M., Rodrigues, H.C., Bendsøe, M.P.: A material optimization model to approximate energy bounds for cellular materials under multiload conditions. Struct. Multidiscip. Optim. **25**, 446–452 (2003)
21. Hackbusch, W.: Integral Equations, vol. 120 of International Series of Numerical Mathematics. Birkhäuser Verlag, Basel (1995)

22. Huyse, L.: Free-form airfoil shape optimization under uncertainty using maximum expected value and second-order second-moment strategies. ICASE report ; no. 2001-18. ICASE, NASA Langley Research Center Available from NASA Center for Aerospace Information, Hampton, VA (2001)
23. Lenz, M.: Modellierung und Simulation des effektiven Verhaltens von Grenzflächen in Metalllegierungen. Dissertation, Universität Bonn (2007)
24. Marsden, J., Hughes, T.: Mathematical Foundations of Elasticity. Dover Publications Inc., New York (1993)
25. Michell, A.: LVIII. The limits of economy of material in frame-structures. Philosophical Magazine Series 6 8, 47, 589–597 (1904)
26. Nocedal, J., Wright, S.J.: Numerical Optimization. Springer Series in Operations Research, Berlin (1999)
27. Penzler, P., Rumpf, M., Wirth, B.: A phase-field model for compliance shape optimization in nonlinear elasticity. ESAIM: COCV **18**(1), 229–258 (2012)
28. Pflug, G.C., Römisch, W.: Modeling, Measuring and Managing Risk. World Scientific, Singapore (2007)
29. Schultz, R., Tiedemann, S.: Conditional value-at-risk in stochastic programs with mixed-integer recourse. Math. Program. **105**(2–3), 365–386 (2006)
30. Shapiro, A., Dentcheva, D., Ruszczyński, A.: Lectures on Stochastic Programming. SIAM-MPS, Philadelphia (2009)
31. Shewchuk, J.: Triangle: engineering a 2d quality mesh generator and delaunay triangulator. Appl. Comput. Geom. Towards Geom. Eng. **1148**, 203–222 (1996)
32. Shewchuk, J.: Delaunay refinement algorithms for triangular mesh generation. Comput. Geom. Theory Appl. **22**, 21–74 (2002)
33. Sokołowski, J., Zolésio, J.-P.: Introduction to Shape Optimization: Shape Sensitivity Analysis. Springer, Berlin (1992)
34. Suzuki, K., Kikuchi, N.: A homogenization method for shape and topology optimization. Comput. Methods Appl. Mech. Eng. **93**(3), 291–318 (1991)
35. Wächter, A.: An Interior Point Algorithm for Large-Scale Nonlinear Optimization with Applications in Process Engineering. Phd thesis, Carnegie Mellon University (2002)
36. Wächter, A., Biegler, L.: On the implementation of a primal-dual interior point filter line search algorithm for large-scale nonlinear programming. Math. Program. **106**(1), 25–57 (2006)
37. Zhuang, C., Xiong, Z., Ding, H.: A level set method for topology optimization of heat conduction problem under multiple load cases. Comput. Methods Appl. Mech. Eng. **196**, 1074–1084 (2007)